

# Eardrum-Inspired Active Sensors for Self-Powered Cardiovascular System Characterization and Throat-Attached Anti-Interference Voice Recognition

Jin Yang, Jun Chen, Yuanjie Su, Qingshen Jing, Zhaoling Li, Fang Yi, Xiaonan Wen, Zhaona Wang, and Zhong Lin Wang\*

By capturing human physiological or behavioral characteristics, wearable electronic sensors in biomonitors and biometric systems carry significant importance in daily life such as in personalized health monitoring and assessment, disease diagnosis, entrance and mobile control, secured financial transactions, and others.<sup>[1–15]</sup> Detected from human skin, the arterial pulse wave and throat sound are typical physiological and behavioral signals acquired for human characterization.<sup>[8–11]</sup> To date, a majority of the wearable pressure sensors are based on force-induced changes in capacitance,<sup>[17–19]</sup> piezoelectricity,<sup>[20–25]</sup> and resistivity,<sup>[26–30]</sup> with various micro/nano architectures.<sup>[31–37]</sup> Despite the potential and high performance, widespread usage of these techniques is possibly limited by structure complexity, fabrication of high-quality materials, reliance on external power source, and the infeasibility of response to high-frequency dynamic pressure, such as sound recovery from throat vibrations that lies in a frequency range of normally higher than 500 Hz.<sup>[9,11]</sup>

Furthermore, a critical weakness of current authentication systems is that an impostor can easily access identification systems to steal the owner's personal information, health record, and even financial data. Biometrics, the reliance on physiological or behavioral characteristics that are unique and exclusive representing features of the genuine owner, has rendered a possible solution to this problem.<sup>[8]</sup> However, all of the current biometrics authentication systems are unimodal, relying on a single source of information to establish an identity, and have limitations like noise in sensed data, intraclass variation, interclass similarity, and nonuniversality and spoof attack.<sup>[9–11]</sup> Thus, a desired identifier based on multiple physiological or behavioral characteristics would be preferred to add multilayers of

strong security to current authentication systems without major modification.

Here, we report the first self-powered bionic membrane sensor (BMS), which is wearable, lightweight, cost-effective, easy to fabricate, and capable of working in a multimodal manner for either health-monitoring or authentication purposes. Innovatively coupling the contact electrification effect<sup>[38–41]</sup> with a structure inspiration by a human eardrum, the as-fabricated BMS holds a superior sensitivity of 51 mV Pa<sup>-1</sup> with a fast response time less than 6 ms as well as a pressure detection limit down to 2.5 Pa. Moreover, a negligible loading–unloading signal change was experimentally observed over 40 000 cycles, indicating its performance stability and durability. In addition, compared with previous pressure sensors,<sup>[5,16,17,25,28,30,33]</sup> the BMS can be utilized to measure rapidly changing pressure over an exceptional wide frequency ranges from 0.1 to 3.2 kHz, which enables it to not only continuously monitor the human low-frequency arterial pulse wave, but also to acquire and recover the high-frequency throat sound using a single device. As a demonstration, first, by measuring the distinguishable dynamic pressure patterns of human cardiovascular system, the BMS is capable of acting as a wearable, mobile, user-friendly, and self-powered arterial pulse wave monitor for continuous and noninvasive human health assessment and monitoring. Second, the BMS is a superior anti-interference throat microphone operating without external power; this self-powered device can pick up and recover human throat voice even in an extremely noisy or windy environment. Third, we innovatively propose a new medical biometric authentication technique by using the arterial pulse wave, which is unique as a medical pattern for authentication. More importantly, for the first time, a multimodal biometric authentication system (MM-BAS) was developed relying on a single BMS, with advantages of low-cost and simplicity in system construction, which exhibits a remarkably lower Equal Error Rate (EER) of 1.6%, compared with the state-of-the-art biometric techniques.<sup>[8–11]</sup> This exceptional achievement is mainly attributed to a fusion of distinguishable physiological pulse wave traits and behavioral throat sound characteristics as a multilayered strong security to defend the MM-BAS. Given the collection of compelling features of the BMS including small volume, light weight, low cost, self-powered, and proven reliability, it not only opens up a new technique in wearable medical/health monitoring, but also it inaugurates the age of high-accuracy single-sensor multimodal biometric authentication.

Dr. J. Yang, J. Chen, Y. Su, Q. Jing, Z. Li, F. Yi, X. Wen, Z. Wang, Prof. Z. L. Wang  
School of Materials Science and Engineering  
Georgia Institute of Technology  
Atlanta, Georgia 30332, USA  
E-mail: zlwang@gatech.edu

Dr. J. Yang  
Department of Optoelectronic Engineering  
Chongqing University  
Chongqing 400044, China  
Prof. Z. L. Wang  
Beijing Institute of Nanoenergy and Nanosystems  
Chinese Academy of Sciences  
Beijing 100083, China



DOI: 10.1002/adma.201404794

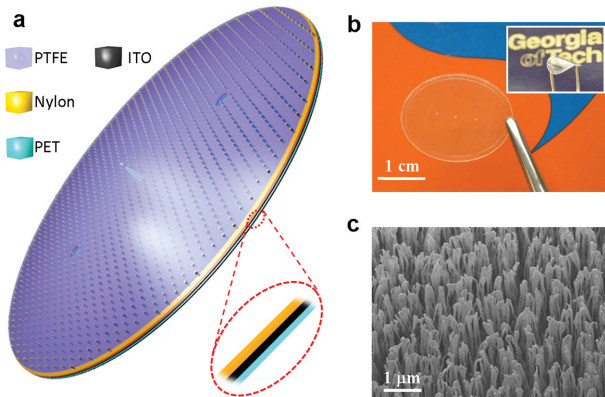


**Figure 1.** Structural design of the bionic membrane sensor. a) Schematic illustrations of the bionic membrane sensor. b) Photograph of an as-fabricated flexible and transparent bionic membrane sensor. The scale bar is 1.0 cm. c) A SEM image of surface-etched PTFE nanowires. The scale bar is 1  $\mu\text{m}$ .

A BMS has a multilayered structure with a thin layer of polyethylene terephthalate (PET) in an oval shape as the bottom supporting substrate, as schematically shown in **Figure 1a**. The oval shape was inspired from the human tympanic membrane, enabling the BMS to monitor the external dynamic pressure with wide frequency range. A layer of indium tin oxide (ITO) coated nylon thin film was laminated onto the PET substrate with the ITO acting as the back electrode and the nylon functioning as one electrification layer. Mimicked a human eardrum, a layer of polytetrafluoroethylene (PTFE) tympanic membrane is tented outwards at the level of the tip of an umbo, which was centered at a nylon layer with a size of  $\Phi 0.6 \times 0.4$  mm. The PET was chosen as the material of the umbo, whose two ends were tightly attached with the PTFE membrane and the nylon layer, respectively. The height of umbo will determine the pressure detection limit as well as detection range of the as-fabricated BMS. By peripherally being anchored, the tensed oval PTFE tympanic membrane, acting as another electrification layer, is extremely sensitive to external dynamic pressure over a wideband frequency range like human eardrum. The formed slightly conical cavity between the PTFE and nylon serves as an air spacer for the charge generation and transfer. And two circular acoustic holes with diameters of 0.5 mm are punched through the PET, ITO, and nylon three layers, acting as communicating vessels to integrate the conical cavity with the ambient air. A photograph of an as-fabricated flexible and transparent BMS is shown in **Figure 1b**. In order to enhance the triboelectrification, vertically aligned polymer nanowires were created onto the PTFE surface for an intimate contact with nylon. A scanning electron microscopy (SEM) image of PTFE nanowires is displayed in **Figure 1c**, which

indicates that the average clustering diameter of nanowires is 110 nm with an average length of 0.8  $\mu\text{m}$ . In general, the surfaces of a nylon and a PTFE film consist of milli/micro/nano hierarchical structure. Without PTFE nanowires, the contact between the nylon and PTFE is not compact at certain points due to the surface morphology and structures, as illustrated in **Figure S1a**, Supporting Information. While with PTFE nanowires, the nanowires are likely to be readily bent and become adaptive to the surface morphology of the nylon for an intimate contact, as schematically demonstrated in **Figure S1b**, Supporting Information. Such a conformable interaction can result in an improvement of the effective contact area, thus improving the output performance. As discussed in methods, the fabrication process of the BMS is straightforward and compatible with possible large-scale manufacturing.

Designed to mimic a human eardrum, the working principle of the BMS can be elucidated in two aspects, namely, membrane mechanical vibration and vibration induced electricity generation. On one hand, the mechanical vibration patterns of the PTFE tympanic membrane in response to external pressure at various frequencies spanning from 100 to 5 kHz were simulated by a finite element analysis, as demonstrated in **Figure 2a**. The simulation is carried out based on an assumption that the applied pressure is uniformly distributed and holds at a constant of 0.6 kPa. Meanwhile, the Young's modulus and Poisson's ratio of the PTFE tympanic membrane are assumed to be 480 MPa and 0.46, respectively. As it can be observed from the simulation results, the deformation regions and magnitudes of PTFE tympanic membrane are highly related to the external excitation frequencies. A frequency response of the BMS was demonstrated in **Figure S2**, Supporting Information. And it

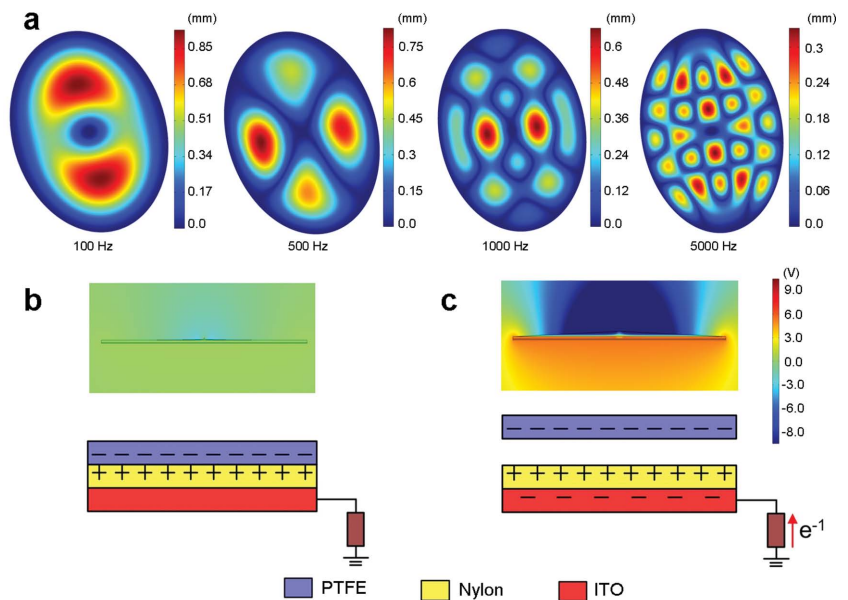


**Figure 2.** Demonstration of the working principle of the bionic membrane sensor. a) The ANSYS software was employed to characterize the PTFE membrane vibrations under various applied pressures at frequencies of 100, 500, 1000, and 5000 Hz, respectively. A PTFE membrane vibration induced electricity generation process was simulated via COMSOL. b) Contact state in which the PTFE is negatively charged, while the nylon is positively charged. c) When the elastic PTFE membrane is released, an emerged potential difference drives free electrons to flow from the ground to ITO electrode through the external circuit.

shows that an extremely wide working bandwidth of 3200 Hz was achieved, which affirms the validity of the BMS structural design mimicking from human eardrum.

On the other hand, the vibration induced electricity generation is attributed to a coupling between contact electrification and electrostatic induction. A cycle of electricity generation process under external pressure is schematically depicted in Figure 2b,c, which is a two-dimensional charge potential distribution by COMSOL. To begin with, when the external pressure brings the PTFE in contact with nylon, since these two materials have a different affinity for electrons, with the PTFE eager to grab electrons and the nylon able to give them up, positive triboelectric charges on the nylon side and negative ones on the PTFE side will be produced. In the current contact state, the generated charges are balanced by their opposite counterparts due to electrostatic induction; consequently, there is neither potential difference across the two layers nor between the ITO electrode and ground (Figure 2b). Once the pressure is released, the PTFE tympanic membrane will immediately rebound back away from the nylon due to its elasticity. A gap will emerge between the two layers, which results in a potential drop across them due to triboelectric charges, so does between the ITO electrode and ground. This is the separation state (Figure 2c). The emerged potential difference drives free electrons to flow from the ground to ITO electrode through the external circuit until it is fully offset.

To characterize the sensing performances of BMS, a computer-controlled linear motor and a force gauge were employed

to provide a well-defined load. At one side of the BMS, a small glass plate with same dimension was placed between the PET substrate and tip of the force gauge. Meanwhile, at another side of the BMS, a polydimethylsiloxane (PDMS) pad was anchored to a linear motor tip to apply the pressures uniformly onto the PTFE tympanic membrane. To begin with, the electrical outputs of BMS with and without nanowires were respectively measured, when a 1.0 kPa pressure was applied. As shown in Figure S1c,d, Supporting Information, the open circuit voltage with nanomaterials modification is improved to about 1.7 times of that of the BMS without nanomaterials surface modification. While an enhancement factor of 1.9 times for the short-circuit current was observed. Then we measured the electrical outputs of BMS as a function of applied dynamic pressure with a constant frequency of 0.3 Hz. In a cycle of the dynamic pressure, increasing and decreasing pressure were realized through a linear motor. The forward and backward voltage–pressure curves of BMS are demonstrated in Figure 3a. While the concrete time profiles of open-circuit voltage and short-circuit current are presented in Figure S3, Supporting Information. It is worth noting that both pressure response curves exhibit two distinct regions with different slopes. In the low pressure region (<1.2 kPa), well-behaved liner variation in the output voltage with pressure gives a superior pressure sensitivity of 51 mV Pa<sup>-1</sup> and a detection limit of 2.5 Pa. While in the high pressure region (>1.2 kPa), a lower pressure sensitivity was experimentally observed. The different sensitivities

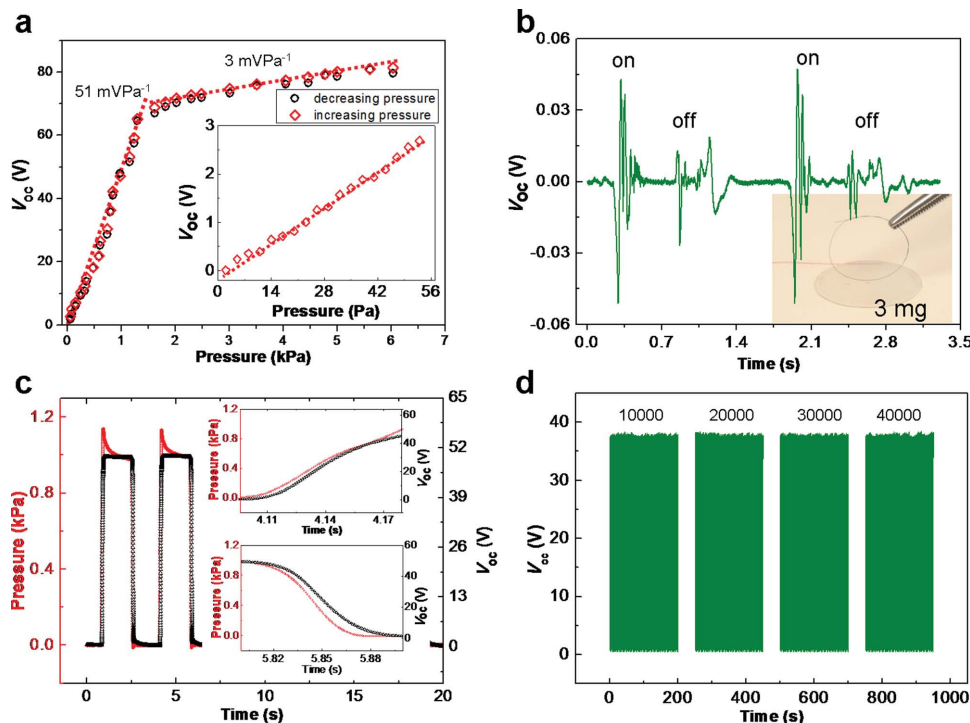


**Figure 3.** Electrical and mechanical characterization of the bionic membrane sensor. a) The electrical characterization of the bionic membrane sensor in response to applied pressure. Inset: enlarged view in small-pressure region from 2.5 to 55 Pa. b) The bionic membrane sensor is able to sense the application of tiny pressures. Shown is the output voltage change on placing and removing a human hair (3 mg). c) Time-resolved sensor response. Periodic pressure changes are utilized to determine the response time taken for the sensor. The enlarged views of the loading and unloading process in one cycle are respectively elucidated in (up) and (down), which renders a response time of less than 6 ms. d) The mechanical durability characterization of the bionic membrane sensor. Under a pressure of 0.8 kPa at a frequency of 2 Hz for 40 000 cycles, no degradation of the output voltage is experimentally observed.

are attributed to a difference of contact area change upon pressure in two distinct regions, that is, in lower pressure region, an equal amount of pressure change results in a larger contact area change, which leads to a higher output voltage increase. Most importantly, relying on an innovative working principle and an unique bio-inspired structure, the BMS distinguishes itself in term of the sensitivity together with the observed broad dynamic range ( $51 \text{ mV Pa}^{-1}$ , in a range of 2.5–1200 Pa), compared with that of other sensors based on capacitive ( $0.55 \text{ kPa}^{-1}$  in units of relative capacitance, in a range of 0.5–2 kPa)<sup>[17]</sup> and piezoelectric ( $0.79 \text{ mV Pa}^{-1}$ , in a range of 0.1–12 Pa).<sup>[25]</sup> Furthermore, for all applied pressures, forward and backward pressure sweep, the forward and backward curves do not show significant hysteresis.

To present a direct view, a 3-mg-human-hair was employed to test the ultrasensitiveness of the BMS, as demonstrated in Figure 3b and Movie 1, Supporting Information. The as-fabricated BMS can reliably detect the placement or removal of the human hair on or from the covered sensor area of  $3.2 \text{ mm}^2$ , corresponding to 13 Pa in contact pressure. The detailed calculation of contact pressure induced by the falling hair is stated in the Supporting Information.

Furthermore, a further step was taken to examine the response time of BMS to external forces. In Figure 3c, a real-time profile of the applied pressure with its corresponding voltage output was demonstrated. Insets are the enlarged views of the loading and unloading process in one cycle, which are respectively elucidated in (up) and (down), rendering a response time of less than 6 ms. This achievement demonstrates a prompt response of the BMS, and is superior to other approaches of its kind in the literature.<sup>[4,17,28,30,33]</sup> A high sensitivity with a fast response time justifies the practicability of BMS for detecting minuscule dynamic pressure, which is of paramount importance for various further applications, such as electronic skin and soft robotics.

In addition, to further investigate the stability of the BMS, a pressure of 0.8 kPa with a frequency of 2 Hz was applied. The voltage was recorded after each 10 000 loading/unloading cycles and 400 cycles of data were presented in each recording, as shown in Figure 3d. The voltage amplitudes exhibit negligible changes after a total 40 000 cycles, revealing a high repeatability, stability, and durability of the BMS.

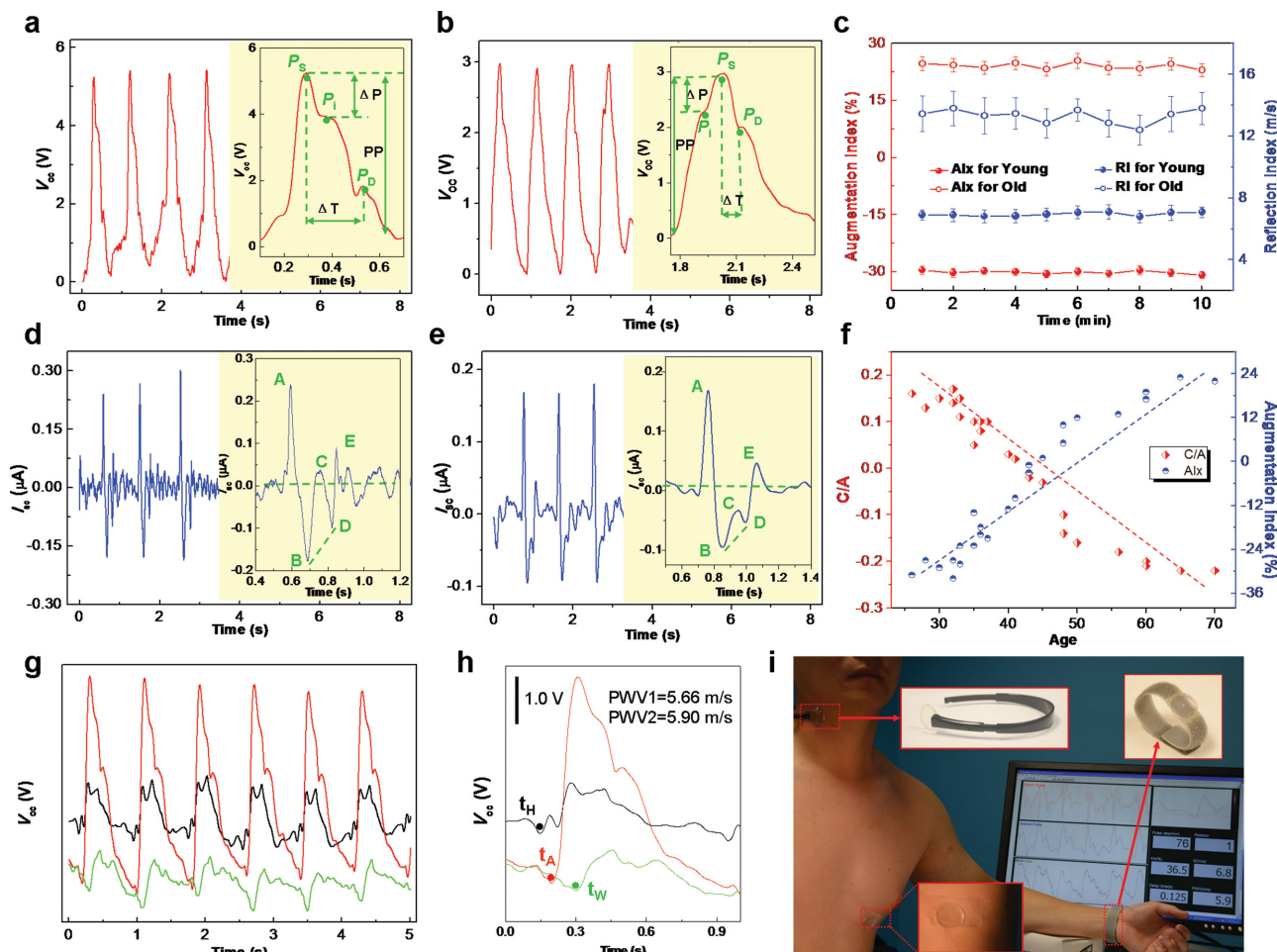
The worldwide leading causes of death are from cardiovascular diseases. Intensive research is focused on early detection and prevention of such diseases, with a special emphasis on arterial compliance capability. Arterial pulse wave propagation in the arterial tree can provide essential information about the arterial physical situation.<sup>[42]</sup> The BMS in this work provides a superior route in acquiring the human arterial pulse wave in a self-powered and noninvasive manner. For a real-time monitoring of the arterial pulse, the BMS was attached onto the carotid, wrist, and chest, just over the artery as it is usually done in arterial tonometry. The arterial pulse wave corresponds to the dynamic pressure change on the skin surface, which can be characterized by the electrical output of the attached BMS.

Figure 4a,b respectively shows the recorded real-time voltages over several pulse periods when a BMS was placed over the carotid arteries of a 30-year-old man and a 70-year-old man. Insets are the enlarged views of one cycle for a detailed

information delivery. A typical characteristic pulse wave shape was obtained with three clearly distinguishable determinants for both the 30-year-old and 70-year-old men: Systolic peak ( $P_S$ ), point of inflection ( $P_i$ ), and dicrotic wave ( $P_D$ ), which are known to be respectively resulted from the blood ejected from the left ventricle, the reflected pulse wave, and the ejected blood back to the left ventricle. A comparison of the pressure pulse waves of a young man with that of an old man indicates apparent differences between the two, especially that  $P_i$  occurs after the  $P_S$  for the younger one, while the  $P_i$  appears before the  $P_S$  for the older one. The differences are significantly related to the physiological condition of human cardiovascular system, which can be quantified by two of the most commonly used parameters:<sup>[42–44]</sup> the augmentation index  $\text{AIx}(\%) = \pm(P_S - P_i)/PP$ , and the reflection index  $\text{RI} = h/\Delta t$ , where  $h$  is the subject height,  $\Delta t$  is the time delay between  $P_S$  and  $P_D$ , while  $PP$  is the absolute pulse wave magnitude. In order to accurately evaluate the physiological conditions of the two peoples' cardiovascular systems, a time period of 10 min was taken to continuously record their arterial pulse waves. Based on the acquired waveforms, a statistical result of the AIx and RI was respectively obtained for the young and old, as shown in Figure 4c. For the younger one, average values of  $-30\%$  and  $6.8 \text{ m s}^{-1}$  were respectively obtained for the parameters AIx and RI, while for the older one, values of  $24.8\%$  and  $13.3 \text{ m s}^{-1}$  were respectively obtained. A distinct difference of AIx and RI between the two subjects is mainly attributed to that, for the young man with better arterial compliance capability, the pulse wave is spread through the arteries at a lower velocity and also the reflected wave arrives back to the aorta after the late systole, resulting in a negative AIx and a smaller RI. In contrast, for the old man with stiffer arteries, the blood pulse velocity is higher and the reflected wave arrives back to the aorta in the early systole, leading to a positive AIx and a larger RI.

Figure 4d,e respectively shows the corresponding real-time current outputs of the 30-year-old man and the 70-year-old man. The inset is an enlarged view of one cycle of the current signal, whose waveform comprises of five main parts, labeled as a-wave to e-wave: initially positive (A-wave), early negative (B-wave), reincreasing (C-wave), late redecaying (D-wave), and diastolic positive (E-wave). The height of each wave was measured from the baseline, with the values above the baseline being positive and those under it negative. A comparison of the current signal waveform of the young man with that of the old man indicates obvious differences between the two, especially that a positive C-wave is observed for the young man, while a negative C-wave for the old one. In order to quantify the difference, a parameter (C/A) was employed, which was defined by the ratio of the height of the C-wave to that of the A-wave. The C/A and AIx values were measured from 25 people with ages spanning from 26 to 70 years old, as shown in Figure 4f. It is interesting to find that the C/A index decreases with age, while AIx follows a reverse trend. These two parameters are reported to independently but complementarily indicate the vascular stiffness, that is, the AIx increases with the increasing of arterial stiffness, while the C/A index decreases. These statistical results highlight that the measured output voltage and current by BMS can reflect the condition of the cardiovascular system as well as the risk of cardiovascular disease. Thus, it can





**Figure 4.** Bionic membrane sensor measured the arterial pulse wave for noninvasive self-powered human health monitoring. a,b) The real-time voltage outputs when the sensors are placed over the carotid arteries of a 30-year-old man and a 70-year-old man, respectively. The inset is an enlarged view of one cycle, which is a graphic representation of the augmentation index (Alx), defined as  $Alx(\%) = \pm(P_S - P_D)/PP$ . PP is the absolute pulse amplitude.  $\Delta t$  is the time delay between the systolic  $P_S$  and diastolic peak  $P_D$ . And thus the reflection index (RI) of carotid artery can be obtained from subject height divided by the time delay. c) Quantitative comparison of the Alx and RI between the 30-year-old man and the 70-year-old one. d,e) The corresponding real-time current outputs of the 30-year-old man and the 70-year-old man, respectively. The inset is an enlarged view of one cycle of the current signal, whose waveform comprises of five main parts, labeled as A-wave to E-wave: initial positive (A-wave), early negative (B-wave), reincreasing (C-wave), late redecaying (D-wave), and diastolic positive (E-wave). f) Relationship between the C/A ratio and Alx in the carotid arteries of 25 subjects aged from 26 to 70 years old. The C/A ratio decreased with age, while Alx followed a reverse trend. g) The pulse waves acquired from three different sites of a participant: carotid artery, left wrist, and the chest. h) An enlarged view of a cycle of output signals corresponding to three positions. And the dots indicate their start points of each cycle. i) A photograph showing the bionic membrane sensors was directly attached to simultaneously monitor the pulse waves of the participant from his carotid artery, chest, and wrist.

be utilized for noninvasive medical diagnosis. The acquired voltage and current signals independently but complementarily give a comprehensive picture of the arterial physical situation.

Meanwhile, in order to obtain more information for cardiovascular risk estimation, a further step was made to measure the pulse wave velocity (PWV) by using multiple BMSs to monitor human pulse waves over different artery sites. The PWV is highly related to the vascular compliance and can be determined by measuring the pulse propagation time from the pressure waveforms at different sites along a vascular segment. A stiffer vessel will conduct the pulse wave faster than a more compliant one. Figure 4g presents the simultaneously acquired voltage signals when three BMSs were respectively attached to the carotid artery, left wrist, and the chest. Figure 4h is enlarged

views of a cycle of output signals, and the characteristic dots indicate their cycle start points. It is worth noting that the start point of the signal acquired from chest comes first, which is 53 and 163 ms earlier than the start points of the signals from the carotid artery and left wrist, respectively. Here, the PWV is derived by dividing the pulse wave propagation distance between the two testing sites by the time delay over that distance. For the test subject,  $PWV1 = 5.66 \text{ m s}^{-1}$  (along chest to carotid artery) and  $PWV2 = 5.9 \text{ m s}^{-1}$  (along chest to left wrist) were experimentally obtained, which are characteristic values expected for a healthy adult.<sup>[43,44]</sup>

To prove the capability of the BMS for self-powered noninvasive arterial pulse measurement, a set of practical applications was demonstrated, as shown in Figure 4i and Movie 2,

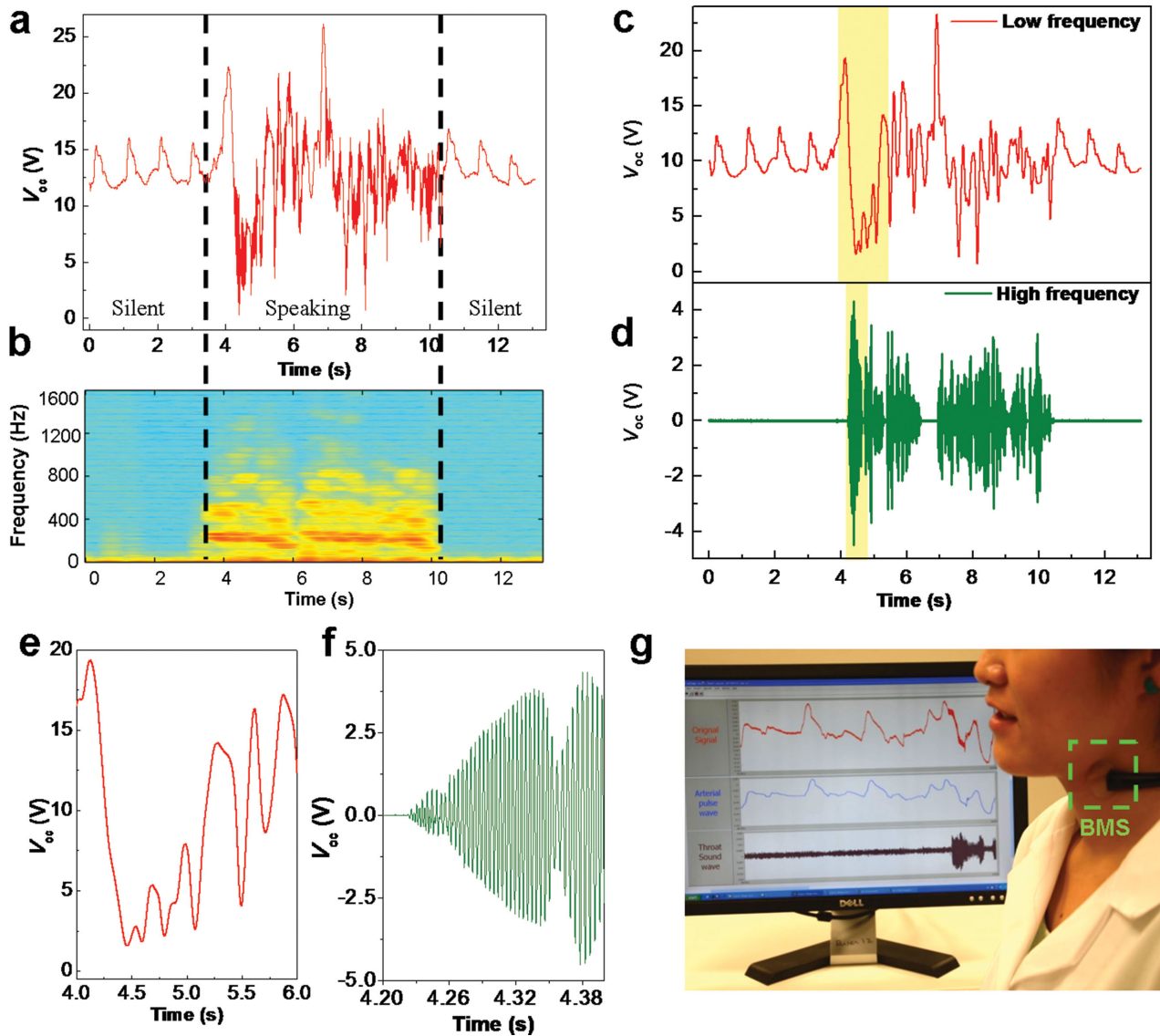


**Figure 5.** Bionic membrane sensor as a superior anti-interference, self-powered, and throat-attached microphone. a) The real-time voltage output in response to the throat vibration during speaking when the sensor is worn against the neck. b) Short-time Fourier transform of the acquired output voltage, which indicates a majority of the frequency components spanning from 45 to 1500 Hz. The low frequency components c) and high frequency components d) of the voltage signal, which are obtained respectively via a 10 Hz-cutoff-frequency low pass filter and a band-pass filter with pass-band from 45 to 1500 Hz. The partial enlarged view of the low frequency component e) and high frequency component f) elaborately illustrates the rich output signals responding to the concrete dynamic change in the speaking, which assures the superior performance of the bionic membrane sensor as a throat microphone. g) A photograph showing the bionic membrane sensor was worn against the participant's neck acting as a self-powered throat microphone.

Supporting Information. Three BMSs were directly attached to simultaneously monitor the pulse waves of the participant from his carotid artery, chest, and wrist, and all of the essential information about the arterial physical situation, including pulse rate, PWV, AIx, and RI, were systematically obtained for a further medical diagnosis.

Throat microphone is becoming more and more popular, since it can effectively pick up speech even in extremely noisy or windy environments, such as for a parachute jumper from the sky, on a motorcycle, or in a busy street, while it is beyond the capability of other types of microphones due to high levels of background noise and the limitation of current technology.

Here, the reported BMS is also capable of acting as superior throat microphone, which is lightweight, small volume, portable, extremely low cost, easy to fabricate, more importantly, it can work without external power. When the BMS was worn against the neck without speaking, a series of pulse waves with low frequency of 1.1 Hz were observed, corresponding to the silent state in Figure 5a. While plentiful high frequency components were emerged and superimposed when the participant spoke the sentence "This is a self-powered throat microphone," which were reflected by the acquired voltage signals in the speaking state in Figure 5a. From the short-time Fourier spectrum of the recorded data, the acquired voltage signal was

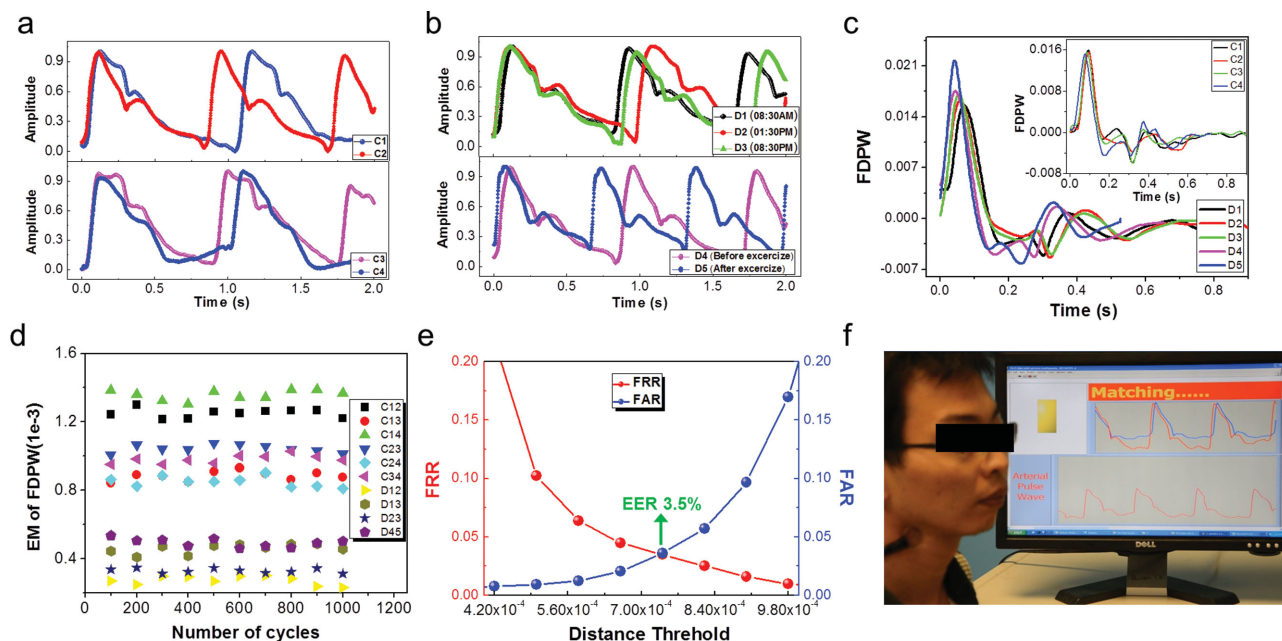


**Figure 6.** Bionic membrane sensor measured the arterial pulse wave for biometric recognition. a) The normalized output voltage measured from the carotid artery of four participants as their heartbeat profiles. b) Heartbeat profiles comparison of a person at different times of a day (up) as well as before and after exercise (down). c) First-derivatives-of-the-pulse-waves (FDPWs) of a person under different activity states. Inset is the FDPWs of the four different participants. d) Calculated Euclidean metrics from the nine FDPWs for a comparison. e) Performance evaluation of the measured heartbeat profiles for biometric authentication. The variation of FAR and FRR in relation to the threshold indicates a low EER value of 3.5% at the threshold of  $7.3 \times 10^{-4}$ . f) A photograph showing the bionic membrane sensor worn on the participant's neck to measure the pulse wave for biometric recognition.

analyzed, obviously indicating a majority of the frequency components spanning from 45 to 1500 Hz when peaking, as shown in Figure 5b. Then, according to the frequency distribution, a 10 Hz cutoff-frequency low-pass finite impulse response digital filter was further used to get the low frequency components from the acquired voltage signal (Figure 5c). While a band-pass finite impulse response digital filter with a pass-band from 45 to 1500 Hz was applied to resolve the throat sound from the acquired voltage signal (Figure 5d). The partial enlarged views of the low frequency component (Figure 5e) and high frequency component (Figure 5f) elaborately illustrate the rich output signals responding to the concrete dynamic change in the speaking, which exhibits plenty high frequency detailed information and thus can be harnessed to rebuild/recover the speaking content, which is beyond the capability of previous report.<sup>[5,30]</sup>

To prove the capability of the BMS as a superior self-powered throat microphone, a practical application was demonstrated, as shown in Figure 5g and Movie 3, Supporting Information. When the tester worn the BMS against her neck and spoke in a noisy environment, the speaking content can be successfully recovered, and it is demonstrated in Audio 1, Supporting Information. This is the first invention that a single self-powered sensor can exhibit a multifunctionality of simultaneously acting as a throat microphone and a noninvasive arterial pulse wave monitor, which will attract extensive attentions, especially for astronauts, soldiers, motorcycle riders, and those who have to keep quiet while communicating with others at a distance, such as during covert military operations.

Biometric recognition, an automatic identification and verification of a person based on the physiological or behavioral

characteristics, is getting increasing research attention for that the current authentication system cannot be easily separated from the genuine owner. Alternative to the traditional approach is medical biometric. The advantage of the bio signal is that it gives some sort of intrinsic characteristics to avoid spoof attack, which can be easily combined with the traditional biometric, such as speech, without any additional cost. Here, we innovatively propose a new medical biometric authentication technique by using the arterial pulse wave.

Due to the ultrasensitiveness of the BMS to external pressure, it can capture plenty of information to fully characterize each one's arterial pulse wave, which thus could be used for further verification and recognition purposes. Figure 6a shows the normalized output voltages measured from the carotid arteries of four participants. A comparison of the obtained four sets of pulse wave patterns indicates explicit differences not only in heart rates, but also in the arterial pulse wave shapes. This is mainly attributed to differences in age, gender, chest configuration, and the position, size, as well as anatomy of the hearts of these individuals.

For quantitative differentiation, Euclidean Metric (EM) was calculated to measure the difference among pulse waves. Two pulse wave signals  $X$  and  $Y$  represent two different individuals. Let  $X_i = [x_{i1}, x_{i2}, \dots, x_{iN}]$  and  $Y_i = [y_{i1}, y_{i2}, \dots, y_{iM}]$  ( $N < M$ ), respectively, denote the  $i$ th cycle of pulse waves  $X$  and  $Y$ . Then the average value of EM between  $X$  and  $Y$  over  $K$  cycles can be defined as follows

$$d_{\mathbf{xy}} = \frac{1}{K} \sum_{i=1}^K \frac{1}{N} \sum_{j=1}^N |x_{ij} - y_{ij}| \quad (1)$$

In the meanwhile, the average value of EM of an individual over different time periods can be expressed as

$$d_{xx} = \frac{1}{K} \sum_{i=1}^K \frac{1}{N} \sum_{j=1}^N |x_{ij} - x_{(i+1)j}| \quad (2)$$

The calculated EM values for a set of four individuals were shown in Figure S5a, Supporting Information, demonstrating that the obtained values of  $d_{XY}$  are much larger than  $d_{XX}$ . Furthermore, the pulse waves also relate to the human activity states, such as emotional fluctuation, exercise, and so on. In this regard, as shown in Figure 6b, the pulse waves of a same person at different times in a day (up) as well as before and after exercise (down) are systematically monitored, and the expected different time profiles are obtained. Likewise, their corresponding EM values were calculated and shown in Figure S5b, Supporting Information. In this regard, a predicament emerges that a few EM values of individual pulse waves under different states are comparable with the EM values of pulse waves among different people. Consequently, it is difficult to distinguish individuals by simply using EMs of the pulse waves. The predicament cannot be walked out by resorting to the First-derivatives-of-the-pulse-waves (FDPWs), which is capable of representing the shape pattern of the pulse wave. Figure 6c shows the FDPWs of the same person under different activity states. Inset is the FDPWs of the four different individuals. Subsequently, a further step was taken to measure and compare the corresponding EMs of the FDPWs, as the results presented in Figure 6d. It is inspiring to note that the EM values of the FDPWs among different individuals are obviously larger than that for the same person under different activity states. As a result, the distinguishable EMs of FDPWs can be used as the feature representation of pulse wave, acting as a threshold to separate the genuine pulse waves from the impostor ones, if an authentication system is established using pulse wave.

To evaluate the identification performance, 120 randomly chosen individuals were invited to record their arterial pulse waves. The collected 120 individual pulse waves were divided

into 60 client patterns and 60 impostor patterns. And the performance of the pulse wave based authentication biometrics is characterized through two error rates: False Rejection Rate (FRR) and False Acceptance Rate (FAR). The variation of FAR and FRR in relation to the threshold is shown in Figure 6e. The FAR is decreasing with the elevated EM of the FDPWs, while FRR follows a reverse trend. However, the FRR and FAR intersect at a certain threshold value of  $7.3 \times 10^{-4}$ , which indicates the EER point of the biometric authentication system with a low EER value of 3.5%.

In addition, to prove the capability of the acquired pulse waves for biometric authentication, a practical application was demonstrated, as shown in Figure 6f and Movie 4, Supporting Information. When four individuals wearing the BMS against the necks, each one can be accurately identified and recognized from the stored templates in computer data base. Acting as a new biometric authentication technique, the measured pulse wave by BMS is an effective identifier, which is reliable, practical, and thus a work toward developing a secured authentication system.

A biometric system that relies only on a single physiological or behavioral characteristic in making a personal identification is often not able to meet the desired performance requirements. Identification based on multiple biometrics represents an emerging trend. Here, relying on the superior sensing performance of BMS, a multimodal biometric authentication system was established using a single BMS, which, for the first time, integrates the pulse wave recognition and voice recognition in making a personal identification.

To demonstrate the capability of BMS for multimodal biometric authentication, a first step was taken here to show its functionality for voice recognition, since the capability of BMS for pulse wave recognition was justified in the previous paragraphs. Figure 7a,b shows the originally recorded voltage signals when two participants were continuously saying "one world" more than three times in each accustomed manner. Figure 7c, d are their corresponding high frequency components of the recorded voltage signals via a 45-to-1500-Hz band-pass filter, which correspond to the throat sound signals according to the

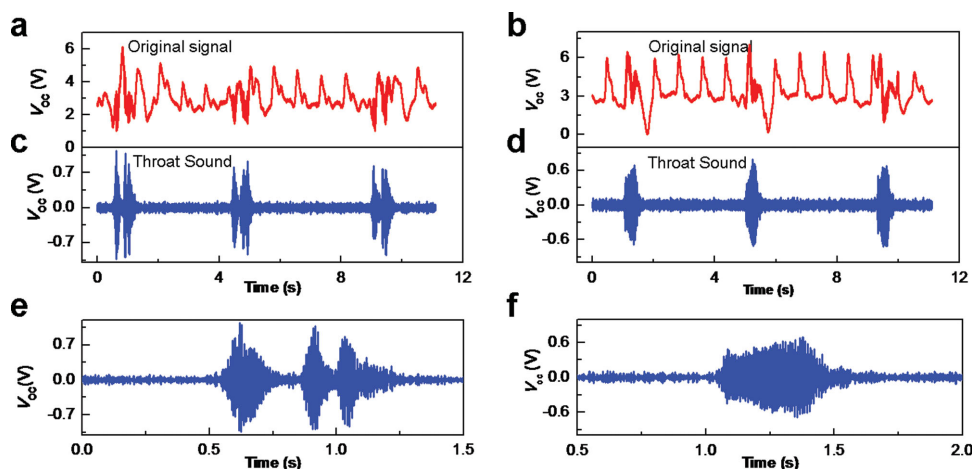


**Figure 7.** Bionic membrane sensor measured throat sound for biometric recognition. a,b) The recorded voltage signals when Alex and Tom were continuously saying "one world" more than three times, respectively. c,d) The high frequency components of the recorded voltage signals from Alex and Tom via a ban-pass filter, respectively. e,f) The enlarged views of a cycle of the high frequency components from Alex and Tom, respectively.



frequency distribution. Enlarged views of one cycle of the voice signal for saying “one world” of two participants are respectively shown in Figure 7e, f. It is clearly noted that these throat sound waves look apparently different from each other, which is mainly attributed to the differences of anatomy (e.g., size and shape of the throat) and behavioral patterns (e.g., voice pitch, speaking style).

Pearson correlation coefficient was utilized to quantitatively measure the difference between two throat sounds signals. Let  $\mathbf{X} = [x_1, x_2, \dots, x_N]$  and  $\mathbf{Y} = [y_1, y_2, \dots, y_N]$  denote two throat sound signals from two different individuals, the Pearson correlation coefficient between signals  $\mathbf{X}$  and  $\mathbf{Y}$  can be defined as

$$r = \frac{\sum_{i=1}^N (x_i - \bar{x})(y_i - \bar{y})}{\sqrt{\sum_{i=1}^N (x_i - \bar{x})^2} \sqrt{\sum_{i=1}^N (y_i - \bar{y})^2}} \quad (3)$$

To evaluate the performance of the BMS for voice recognition, 120 participants were invited to independently say the phrase “one world” for more than four times in each accustomed manner with the BMS wearing against the necks. A calculation of the Pearson correlation coefficient between any two of the throat sound signals of 120 participants was performed, and the results were demonstrated in Figure 8a. It is worth noting that most of the Pearson correlation coefficients from

individual self-comparing are larger than 0.7, while the Pearson correlation coefficients from comparison among individuals are less than 0.7, which is indicative of that Pearson correlation coefficient can be harnessed to act as a threshold to separate the genuine voice from the impostor voice, if a verification system is thus established. The variation of FAR and FRR in relation to the threshold is shown in Figure 8b. The presented BMS based voice authentication system achieves an EER value of 2.7% at the threshold of 0.55.

For an enhanced authentication performance, identification based on the integration of the pulse wave and voice recognition was evaluated as a multimodal biometric. The new feature representation for the multimodal biometric authentication system is a combination of EM of the FDPWs ( $d_{XY}$ ) from the pulse wave recognition and Pearson correlation coefficient ( $r$ ) from the voice recognition. And the new feature representation is mathematically expressed by a feature vector  $\mathbf{T} = [d_{XYi}, r_i]$ , where  $i = 1, 2, 3, \dots, u$ , denoting the index of the user ( $u$  is total number of users in the system database). A new threshold relying on the feature vector can be defined as

$$TSM_i = w_1 \times 0.0018 / d_{xyi} + w_2 r_i \quad (4)$$

The weight coefficients  $w_1$  and  $w_2$  are proportional to the authentication performance of the two unimodal systems with a constraint of  $w_1 + w_2 = 1$ . A larger value of  $TSM_i$  indicates a larger similarity between the user templates and client

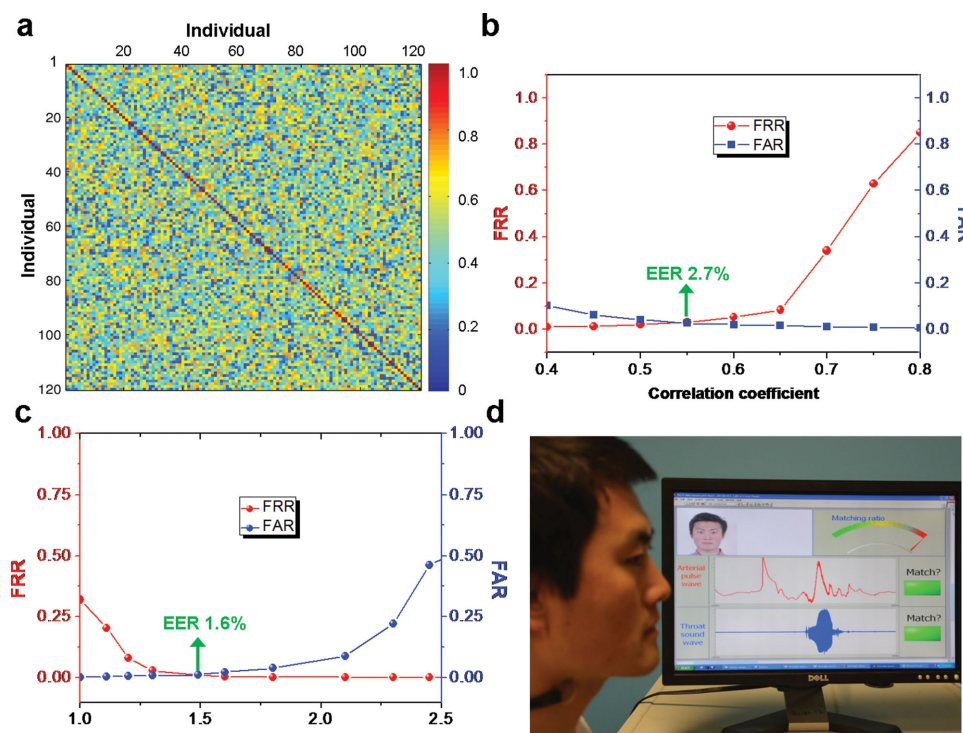


**Figure 8.** Bionic membrane sensor simultaneously recorded the arterial pulse and throat sound for single-sensor multimodal biometric authentication. a) Calculated correlation coefficients of the throat sounds among different individuals as well as the same individual. b) Performance evaluation of the measured throat sound profiles for biometric authentication, which indicates a low EER value of 2.7% at the threshold of 0.55. c) Performance evaluation of the presented multimodal biometric authentication system. The variation of FAR and FRR in relation to the threshold, which indicates a remarkably low EER value of 1.6% at the threshold of 1.5. d) A photograph showing the bionic membrane sensor was worn against the participant’s neck to simultaneously record the arterial pulse and throat sound for a single-sensor multimodal biometric authentication.

templates. As demonstrated in Figure 8c, a remarkably low EER value of 1.6% was achieved for the presented multimodal biometric authentication system at a threshold value of 1.5. As demonstrated in Figure 8d and Movie 5, Supporting Information, the BMS was utilized for a multimodal biometric authentication, by simultaneously recording the arterial pulse and throat sound, and only the genuine owner with matched both arterial pulse wave and throat sound can access into the computer. Given its authentication ability, a BMS is capable of simultaneously identifying personal characters physiologically as well as behaviorally. The results demonstrate that the identity established by such an integrated system is much more reliable than the identity established by a single biometrics, making it unique and practical for developing a highly secured biometrics authentication system.

Compared with other existing technologies for wearable electronic sensors in biomonitoring and biometric systems, the BMS is distinct and unique in fundamental mechanism. Utilizing triboelectrification, a universally applicable charging effect that is confined only at contact surfaces, the BMS distinguishes itself in term of performance in a number of major aspects.

From the performance point of view, innovatively harnessed the ubiquitous contact electrification and the structural bioinspiration from human eardrum, the as-fabricated BMS holds a collection of superior performance, including superior stability, high sensitivity together with the observed broad dynamic range ( $51 \text{ mV Pa}^{-1}$ , in a range of 2.5–1200 Pa), fast response time of less than 6 ms, low pressure detection limit down to 2.5 Pa, and wide working bandwidth of 0.1 Hz to 3.2 kHz for measuring rapidly changing pressure. The sensing characteristics assure extensive applications of BMS with guaranteed performances. First, the BMS is capable of acting as a wearable, mobile, user-friendly, and self-powered arterial pulse wave monitor for continuous and noninvasive human health assessment. Second, the BMS is a superior anti-interference throat-attached microphone operating without external power source, which can pick up and recover human throat voice even in extremely noisy, windy environments, or even voiceless environment based on through vibration. Third, by measuring the distinguishable dynamic pressure patterns of human cardiovascular system, the BMS creates a new medical biometric authentication technique by using the arterial pulse wave. More importantly, for the first time, a less intrusive, high-authentication-accuracy single-sensor MM-BAS was developed with a lower EER value of 1.6%.

From the cost point of view, consisting of only transparent thin film materials, the BMS is extremely low-cost, lightweight, flexible, excellent machinability. First, due to surface charging effect, the fabrication of the BMS requires only very small amount of materials, which are conventional polymers or very thin layer of ITO as electrodes. Second, the fabrication process of the BMS is straightforward and compatible with large-scale manufacturing, such as laser cutting and layer lamination. As a consequence, the reported BMS in this work is cost-effective and suitable for mass production. Given a collection of compelling features of the BMS including self-powered, lightweight, simplicity in device fabrication, high price to performance ratio and proven reliability, the justified concepts and demonstrations in this work can be immediately and extensively adopted in a variety of applications in wearable medical/health

monitoring as well as biometric authentication, and come into effect of improving the way of our living.

## Experimental Section

**Fabrication of Nanowires Array on PTFE Surface:** A PTFE film with 25- $\mu\text{m}$ -thickness was first cleaned subsequently by menthol, isopropyl alcohol, and deionized water. Then, the inductively coupled plasma (ICP) reactive ion etching was used to fabricate the aligned nanowires on the PTFE surface.  $\text{O}_2$ , Ar, and  $\text{CF}_4$  gases were injected into the ICP chamber with a flow ratio of 10.0, 15.0, and 30.0 sccm, respectively. A large density of plasma was produced by a power source of 400 W. And another power source of 100 W was used to accelerate the plasma ions. The PTFE nanowires with an average length of  $\approx 0.8 \mu\text{m}$  were obtained after the PTFE was etched for 60 s.

**Fabrication of a BMS:** (1) A layer of 100 nm ITO was deposited onto the backside of nylon as electrode. Then the nylon layer and a layer of PET (thickness 75  $\mu\text{m}$ ) were cut into oval shapes with the semi-major axis of 1.25 cm and the semi-minor axis of 1 cm using a laser cutter. (2) Adhere the nylon on one side of the PET with ITO-coated side facing PET. (3) Two circular acoustic holes with diameter of 0.5 mm are fabricated and punched through the PET, ITO, and nylon layers using laser cutter, which are symmetrically located on both sides of the oval center along the major axis with a distance of 10 mm. (4) A tiny umbo ( $\Phi 0.6 \times 0.4 \text{ mm}$ ) is attached to the center of the top side of the nylon film, then a layer of PTFE film (thickness 25  $\mu\text{m}$ ) is anchored at the boundary of the top side of the nylon. As a result, the PTFE membrane can be embossed by the tiny umbo, enabling it to maintain elastic tension.

**Fabrication of a PDMS Pad:** A PDMS elastomer and cross-linker (Sylgard 184, Dow Corning) were mixed with a 10:1 mass ratio and stirred for 10 min. The mixture was then evacuated at room temperature for 20 min to remove the gas bubbles. After that, it was casted onto a relatively rigid, pre-cleaned polyethylene terephthalate (PET) plate and kept in the oven at 65 °C for 1 h to get cured. Subsequently, one surface of the PDMS layer was coated with a layer of copper thin film.

**Experimental Setup for Pressure Measurement:** (1) Mount our BMS vertically on a three-dimensional positioner that also has control on rotation and tilt. (2) Align and connect the small glass plate with a force sensor. (3) Vertically mount the PDMS pad to one end of a linear motor for reciprocating motion. (4) Adjust the three-dimensional positioner so that the BMS surface and the PDMS pad surface are parallel to each other. (5) Simultaneously monitor the BMS output using an electrometer and the interaction force between BMS and the glass plate. (6) Change the interaction force through incrementally changing stroke distance of the linear motor to investigate the dependence of voltage on different applied pressures.

**Experimental Setup for the Electrical Measurement:** (1) A dual-range force sensor (Vernier Software & Technology, LLC.) was employed to measure the applied force by a linear motor to the BMS. (2) The output voltage signal of the BMS was acquired via a voltage preamplifier (Keithley 6514 System Electrometer). The output current signal of the BMS was acquired by a low-noise current preamplifier (Stanford Research SR560).

## Supporting Information

Supporting Information is available from the Wiley Online Library or from the author.

## Acknowledgements

J.Y. and J.C. contributed equally to this work. This work was supported by the U.S. Department of Energy, Office of Basic Energy Sciences

(DE-FG02-07ER46394), the “Thousands Talents” program for pioneering researchers and their innovation team, China, and the NSFC (Grant No. 61174017). We thank Dr. Ying Liu and Yufang Li for assistance with filming the movies in the Supporting Information. Experiments with human subjects were obtained from the individuals with signed consent. Note: The text in the acknowledgements was revised on February 19, 2015, after initial publication online.

Received: October 16, 2014

Revised: November 14, 2014

Published online: January 12, 2015

- [1] Z. Q. Ma, *Science* **2011**, *333*, 830.
- [2] J. Y. Sun, C. Keplinger, G. M. Whitesides, Z. Suo, *Adv. Mater.* **2014**, DOI: 10.1002/adma.201403441.
- [3] W. Z. Wu, X. N. Wen, Z. L. Wang, *Science* **2013**, *340*, 952.
- [4] G. Schwartz, B. C. K. Tee, J. Mei, A. L. Appleton, D. H. Kim, H. Wang, Z. N. Bao, *Nat. Commun.* **2013**, *4*, 1859.
- [5] C. Dagdeviren, Y. W. Su, P. Joe, R. Yona, Y. Liu, Y. S. Kim, J. A. Rogers, *Nat. Commun.* **2014**, *5*, 4496.
- [6] M. L. Hammock, A. Chortos, B. C. K. Tee, J. B. H. Tok, Z. N. Bao, *Adv. Mater.* **2013**, *25*, 5997.
- [7] P. Lin, F. Yan, *Adv. Mater.* **2012**, *24*, 34.
- [8] A. K. Jain, A. Ross, S. Prabhakar, *IEEE Trans. Circuits Syst. Video Technol.* **2004**, *14*, 4.
- [9] J. A. Unar, W. C. Seng, A. Abbasi, *Pattern Recognit.* **2014**, *47*, 2673.
- [10] S. K. R. Nair, B. Bhanu, S. Ghosh, N. S. Thakoor, *Pattern Recognit.* **2014**, *47*, 3379.
- [11] M. D. Bugdol, A. W. Mitas, *Pattern Recogn. Lett.* **2014**, *38*, 107.
- [12] T. Someya, Y. Kato, T. Sekitani, S. Iba, Y. Noguchi, Y. Murase, T. Sakurai, *Proc. Natl. Acad. Sci. USA* **2005**, *102*, 12321.
- [13] V. Maheshwari, R. F. Saraf, *Science* **2006**, *312*, 1501.
- [14] T. Sekitani, Y. Noguchi, K. Hata, T. Fukushima, T. Aida, T. Someya, *Science* **2008**, *321*, 1468.
- [15] D. H. Kim, J. H. Ahn, W. M. Choi, H. S. Kim, T. H. Kim, J. Song, J. A. Rogers, *Science* **2008**, *320*, 507.
- [16] M. Kaltenbrunner, T. Sekitani, J. Reeder, T. Yokota, K. Kuribara, T. Tokuhara, T. Someya, *Nature* **2013**, *499*, 458.
- [17] S. C. Mannsfeld, B. C. Tee, R. M. Stoltenberg, C. V. H. Chen, S. Barman, B. V. Muir, Z. N. Bao, *Nat. Mater.* **2010**, *9*, 859.
- [18] D. J. Lipomi, M. Vosgueritchian, B. C. Tee, S. L. Hellstrom, J. A. Lee, C. H. Fox, Z. N. Bao, *Nat. Nanotechnol.* **2011**, *6*, 788.
- [19] D. J. Cohen, D. Mitra, K. Peterson, M. M. Maharbiz, *Nano Lett.* **2012**, *12*, 1821.
- [20] Z. L. Wang, J. H. Song, *Science* **2006**, *312*, 242.
- [21] R. S. Yang, Y. Qin, L. M. Dai, Z. L. Wang, *Nat. Nanotechnol.* **2008**, *4*, 34.
- [22] S. Xu, Y. Qin, C. Xu, Y. G. Wei, R. S. Yang, Z. L. Wang, *Nat. Nanotechnol.* **2010**, *5*, 366.
- [23] D. Mandal, S. Yoon, K. J. Kim, *Macromol. Rapid Commun.* **2011**, *32*, 831.
- [24] X. Xiao, L. Yuan, J. Zhong, T. Ding, Y. Liu, Z. Cai, Z. L. Wang, *Adv. Mater.* **2011**, *23*, 5440.
- [25] L. Persano, C. Dagdeviren, Y. Su, Y. Zhang, S. Girardo, D. Pisignano, J. A. Rogers, *Nat. Commun.* **2013**, *4*, 1633.
- [26] T. Yamada, Y. Hayamizu, Y. Yamamoto, Y. Yomogida, A. Izadi-Najafabadi, D. N. Futaba, K. Hata, *Nat. Nanotechnol.* **2011**, *6*, 296.
- [27] K. Takei, T. Takahashi, J. C. Ho, H. Ko, A. G. Gillies, P. W. Leu, A. Javey, *Nat. Mater.* **2010**, *9*, 821.
- [28] C. Pang, G. Y. Lee, T. I. Kim, S. M. Kim, H. N. Kim, S. H. Ahn, K. Y. Suh, *Nat. Mater.* **2012**, *11*, 795.
- [29] B. C. Tee, C. Wang, R. Allen, Z. N. Bao, *Nat. Nanotechnol.* **2012**, *7*, 825.
- [30] X. Wang, Y. Gu, Z. Xiong, Z. Cui, T. Zhang, *Adv. Mater.* **2014**, *26*, 1336.
- [31] Q. Gao, H. Meguro, S. Okamoto, M. Kimura, *Langmuir* **2012**, *28*, 17593.
- [32] H. B. Yao, J. Ge, C. F. Wang, X. Wang, W. Hu, Z. J. Zheng, S. H. Yu, *Adv. Mater.* **2013**, *25*, 6692.
- [33] S. Gong, W. Schwalb, Y. Wang, Y. Chen, Y. Tang, J. Si, W. Cheng, *Nat. Commun.* **2014**, *5*, 3132.
- [34] L. Pan, A. Chortos, G. Yu, Y. Wang, S. Isaacson, R. Allen, Z. N. Bao, *Nat. Commun.* **2014**, *5*, 3002.
- [35] S. Xu, Y. Zhang, L. Jia, K. E. Mathewson, K. I. Jang, J. Kim, J. A. Rogers, *Science* **2014**, *344*, 70.
- [36] C. Wang, D. Hwang, Z. Yu, K. Takei, J. Park, T. Chen, A. Javey, *Nat. Mater.* **2013**, *12*, 899.
- [37] J. W. Jeong, W. H. Yeo, A. Akhtar, J. J. Norton, Y. J. Kwack, S. Li, J. A. Rogers, *Adv. Mater.* **2013**, *25*, 6839.
- [38] H. T. Baytekin, A. Z. Patashinski, M. Branicki, B. Baytekin, S. Soh, B. A. Grzybowski, *Science* **2011**, *333*, 308.
- [39] F. R. Fan, Z. Q. Tian, Z. L. Wang, *Nano Energy* **2012**, *1*, 328.
- [40] J. Chen, G. Zhu, W. Yang, Q. Jing, P. Bai, Y. Yang, T. C. Hou, Z. L. Wang, *Adv. Mater.* **2013**, *25*, 6094.
- [41] G. Zhu, J. Chen, T. Zhang, Q. Jing, Z. L. Wang, *Nat. Commun.* **2014**, *5*, 3426.
- [42] A. P. Avolio, M. Butlin, A. Walsh, *Physiol. Meas.* **2010**, *31*, R1.
- [43] S. J. Denardo, R. Nandyala, G. L. Freeman, G. L. Pierce, W. W. Nichols, *Heart Failure* **2010**, *3*, 149.
- [44] W. W. Nichols, *Am. J. Hypertens.* **2005**, *18*, 3.